



Polarization analysis by means of individual soft x-ray absorption spectra of rare earthsGerrit van der Laan ^{1,*}, Thorsten Hesjedal ² and Peter Bencok¹¹*Diamond Light Source, Harwell Science and Innovation Campus, Didcot OX11 0DE, United Kingdom*²*Department of Physics, Clarendon Laboratory, University of Oxford, Oxford OX1 3PU, United Kingdom*

(Received 28 August 2022; revised 1 November 2022; accepted 13 December 2022; published 19 December 2022)

X-ray magnetic circular dichroism (XMCD), which by virtue of the sum rules provides element-specific spin and orbital moments, is obtained from the difference between two polarized spectra by reversing the direction of either the light helicity or the applied magnetic field. Usually, it is tacitly assumed that these two spectra are obtained using the same absolute degree of light and magnetic polarization. This is, however, not always possible and depends on circumstances that can be beyond control. First, we recapitulate the conventional XMCD sum rule method to obtain the values of the moments and emphasize some of the complications in the case of the rare-earth $M_{4,5}$ edges, such as the presence of strong core-hole jj overlap, linear dichroism, and magnetic dipole term $\langle T_z \rangle$. Instead, we propose an alternative method. Using the individual polarized x-ray absorption spectra obtained at the Ho and Dy M_5 edges, where each of the $\Delta J = -1, 0,$ and $+1$ transitions are separated by ~ 2 eV in photon energy, we are able to determine independently the degree of circular dichroism in a single spectrum. Since light is a transverse wave, we need to include, apart from the circular dichroism, also a linear dichroism contribution in order to fit the circularly polarized spectra. In the measurements on paramagnetic rare-earth dopants it was found that reversing the field produces the same degree of circular dichroism, while reversing the helicity yields a $\sim 20\%$ difference in the degree of circular dichroism.

DOI: [10.1103/PhysRevB.106.214423](https://doi.org/10.1103/PhysRevB.106.214423)**I. INTRODUCTION**

It has been known since the eighties that the x-ray absorption edge structure of a magnetic material can exhibit a strong polarization dependence [1–3]. The observed x-ray circular and linear magnetic dichroism (XMCD and XMLD) are linear and quadratic proportional, respectively, to the magnetic moment [4]. Analysis of these measurements has made considerable headway thanks to the discovery of the sum rules [5–7], which offer an element- and shell-specific tool for the determination of the ground-state spin- and orbital moments of the local electronic structure in magnetic materials.

Today's undulators in the soft x-ray region are expected to produce almost pure left and right circular as well as variable linear polarization. Knowledge of the degree of polarization is essential to carry out a precise analysis of dichroic and chiral experiments. The degree of polarization can be calibrated using x-ray polarimeters that have been developed at various synchrotron facilities [8,9]. The disadvantage of this kind of polarization characterization is that it not only requires such a dedicated polarimeter but also demands complex data analysis to extract the Stokes parameters. Therefore, these calibrations are usually not done routinely.

Here we present the results of a simple method for the determination of the degree of polarization, which is based on the energy separation between the three different allowed dipole transitions $\Delta J = 0, \pm 1$ in the soft x-ray absorption spectrum. Whereas this would not be a good property of the $L_{2,3}$ edges of the $3d$ transition metals [10], the M_5 edges ($3d \rightarrow 4f$ transitions) of the heavy rare earths (1300–1600 eV) fulfill this requirement to a lesser or greater degree [11]. In some cases, such as for $\text{Yb}^{3+} f^{13}$, not all three transitions are allowed. Most suitable are the M_5 spectra of the Dy f^9 and Ho f^{10} configurations, which resemble each other in spectral appearance, as was already recognized by Thole *et al.* [11]. These M_5 edges show a well-resolved energy splitting with ~ 2 eV between each of the three polarized peaks (Fig. 1).

In this paper, we compare the measured polarized x-ray absorption spectra (XAS) of Dy and Ho with theoretical spectra in order to determine the degree of circular dichroism. There is a good agreement between experimental and theoretical spectra, except for a broad, but low-intensity, structure with distinct polarization at ~ 3 eV above the main peak, absent in the atomic calculation.

II. SUM RULES IN $4f$ METALS

While the sum rules have been extensively applied to $3d$ transition-metal compounds [4], this has been done less so to study rare-earth compounds. The theoretical limitations and experimental restrictions of the sum rules have been summarized in Ref. [12]. Here we revisit more specifically some of the limitations in the particular case of the rare earths.

*Corresponding author: gerrit.vanderlaan@diamond.ac.uk

The sum rules for the $M_{4,5}$ edges of $4f$ metals, which relate the integrated intensities ρ to the ground state expectation values of the orbital moment $\langle L_z \rangle$, spin moment $\langle S_z \rangle$, and magnetic dipole term $\langle T_z \rangle$, can be written in compact form as

$$\frac{\rho_{M_5}^1 + \rho_{M_4}^1}{\rho_{M_5}^0 + \rho_{M_4}^0} = \frac{1}{3} \frac{\langle L_z \rangle}{n_h}, \quad (1)$$

$$\frac{\rho_{M_5}^1 - \frac{3}{2}\rho_{M_4}^1}{\rho_{M_5}^0 + \rho_{M_4}^0} C = \frac{2}{3} \frac{\langle S_{z,\text{eff}} \rangle}{n_h} = \frac{2}{3} \frac{[\langle S_z \rangle + 3\langle T_z \rangle]}{n_h}, \quad (2)$$

where $\rho^0 = \rho_{-1} + \rho_0 + \rho_1$ and $\rho^1 = \rho_{-1} - \rho_1$ are the integrated intensities of the isotropic spectrum and XMCD over the M_5 and M_4 edges. The ρ_q are the integrated intensities of the spectra for left-circular ($q = -1$), right-circular ($q = +1$), and linear *perpendicular* polarization ($q = 0$), respectively. The origin of the correction factor C , appearing in Eq. (2), will be addressed further down.

The number of f holes, $n_h = (14 - n)$, is often a known integer in the case of the rare earths [11]. It cancels out in the orbital-to-spin moment ratio,

$$\frac{\langle L_z \rangle}{\langle S_{z,\text{eff}} \rangle} = \frac{2}{C} \frac{\rho_{M_5}^1 + \rho_{M_4}^1}{\rho_{M_5}^1 - \frac{3}{2}\rho_{M_4}^1}. \quad (3)$$

Sometimes the sum rule analysis is presented in an alternative notational form by using $m_L = -\langle L_z \rangle$, $m_{S,\text{eff}} = -2\langle S_{z,\text{eff}} \rangle$, $p = \rho_{M_5}^1$, $q = \rho_{M_5}^1 + \rho_{M_4}^1$, and $r = \rho_{-1} + \rho_{+1} \equiv \frac{2}{3}\rho^0/R$, where R is a correction factor for the integrated intensities. For instance, Chen *et al.* [13] conveniently assume that there is no linear dichroism, so that $\rho_0 = \frac{1}{2}(\rho_{-1} + \rho_{+1})$, in which case $R = 1$. However, for rare earths the large linear dichroism cannot be neglected and should be included.

This alternative notation rewrites the sum rules as

$$m_L = -2q \frac{n_h}{rR}, \quad (4)$$

$$m_{S,\text{eff}} = -(5p - 3q) \frac{Cn_h}{rR}, \quad (5)$$

$$\frac{m_L}{m_{S,\text{eff}}} = \frac{2}{[5(p/q) - 3]C}, \quad (6)$$

or equivalent to the last equation,

$$\frac{p}{q} = \frac{3}{5} + \frac{2}{5} \frac{m_{S,\text{eff}}}{m_L} \frac{1}{C}. \quad (7)$$

In Eq. (6) the orbital to spin moment ratio is expressed as a function of the branching ratio p/q of the XMCD. This emphasizes the fact that only one variable is needed. As an example, the Hund's rule ground state f^{13} ($^2F_{7/2}$), with one hole in the $J = -7/2$ level, has $L_z = -3$, $S_z = -1/2$, and $T_z = -1/3$, and from Eq. (7) we find $p/q = 1$. This means the XMCD for the M_4 edge is zero, which chimes with the fact that the transition $3d_{3/2} \rightarrow 4f_{7/2}$ is dipole forbidden.

The spin sum rule requires separate integrations over the M_5 and M_4 edge. Therefore, this rule is only strictly valid if the core-level angular momentum j is a good quantum number, which is only true when the core spin-orbit splitting is much larger than the core and valence electrostatic interactions. In that case the correction factor C , introduced in Eq. (2), is

equal to 1 and can be omitted. This condition holds to a good degree for the Fe, Co, and Ni $L_{2,3}$ edges, but a large correction factor is needed for Mn [14], Cr [15], and lighter $3d$ elements. The same problem occurs for the rare earths. As an indication, the values of the correction factor C adopted from Ref. [16] are given in Table I. C scales approximately linearly with the scalings factor of the $3d$ - $4f$ Coulomb and exchange interactions [10].

The deviation in the branching ratio p/q from their real value, ascribed to the spectral overlap of the $3d_{5/2}$ and $3d_{3/2}$ manifolds, increases from f^1 to f^5 since the multiplet width of the f^n increases, which is reflected in the values of C in Table I. The multiplet structure is not only the part that can be reached by the electric dipole transitions but spans a much wider energy than what is visible as the spectrum [10].

III. METHODS

A. Rare-earth-doped samples

The choice of the sample for our demonstration is not critical, although it is preferable to use a dilute sample in order to avoid the strong saturation effects in the soft x-ray absorption. For the measurements we chose rare-earth-doped topological insulator (TI) Bi_2Te_3 samples. TIs have been at the center of interest for unlocking novel physical effects and spin-based electronics alike, owing to their unique electronic properties [17,18]. The gapless topological surface state (TSS) of three-dimensional (3D) TIs, with its counterpropagating streams of oppositely spin-polarized electrons, is protected by time-reversal symmetry (TRS) against backscattering, thereby resulting in high mobilities.

Previously, we reported XMCD studies on transition-metal and rare-earth-doped TIs for Mn-doped Bi_2Se_3 [19] and Bi_2Se_3 [20], Cr-doped Bi_2Se_3 [15,21] and Sb_2Te_3 [22,23], Gd-doped Bi_2Te_3 [24], Ho-doped Bi_2Te_3 [25,26], and Dy-doped Bi_2Te_3 [27,28].

Here we use a $(\text{Ho}_x\text{Bi}_{1-x})_2\text{Te}_3$ thin film with $x = 0.14$, denoting the substitutional Ho concentration, grown on c -plane sapphire using molecular beam epitaxy (MBE). This Ho sample comes from the same batch as that used in Ref. [26]. Details of the thin-film growth and structural and magnetic properties can be found in Refs. [25] and [26]. We also measured a $(\text{Dy}_x\text{Bi}_{1-x})_2\text{Te}_3$ thin film, with $x = 0.113$, which was grown by MBE on c -plane sapphire substrate. It comes from the same batch as in Ref. [27].

B. X-ray magnetic circular dichroism

1. Experimental

XAS at the Dy and Ho $M_{4,5}$ edges were carried out in 5 T field at a temperature of 2.5 K on beamline I10 (BLADE) at the Diamond Light Source, Oxfordshire, using a UHV-compatible 14 T superconducting magnet with liquid He variable temperature insert [4]. The 5 T field is sufficient to fully saturate the magnetization of the Ho- and Dy-doped TIs at 2.5 K (see superconducting quantum interference device (SQUID) results for the Ho sample in Fig. 3 of Ref. [25]). The magnetization of the paramagnetic material vanishes at remanence.

TABLE I. Expectation values $\langle L_z \rangle$, $\langle S_z \rangle$, $\langle T_z \rangle$ and the correction factor $[(S_z) + 3(T_z)]/\langle S_z \rangle$ for the Hund's rule ground states $LSJ(M = -J)$ of the configurations f^n . Also given are the ratio p/q and correction factor C for each element. The sign of $\langle J_z \rangle = \langle L_z \rangle + \langle S_z \rangle$ has been chosen negative.

R^{3+}	n	$\langle L_z \rangle$	$\langle S_z \rangle$	$\langle T_z \rangle$	$\langle S_{z,\text{eff}} \rangle / \langle S_z \rangle$	p/q	C
Ce $f^1 \ ^2F_{5/2}$	1	-20/7	5/14	4/7	5.8	0.02	1.597
Pr $f^2 \ ^3H_4$	2	-24/5	4/5	104/255	2.733	0.236	1.779
Nd $f^3 \ ^4I_{9/2}$	3	-63/11	27/22	21/121	1.424	0.356	2.076
Pm $f^4 \ ^5I_4$	4	-28/5	8/5	-28/165	0.682	0.444	2.498
Sm $f^5 \ ^6H_{5/2}$	5	-30/7	25/14	-26/33	-0.324	0.708	3.350
Eu $f^6 \ ^7F_0$	6	0	0	0	-	-	-
Gd $f^7 \ ^8S_{7/2}$	7	0	-7/2	0	1	-	0.949
Tb $f^8 \ ^7F_6$	8	-3	-3	1/3	0.667	1.133	0.882
Dy $f^9 \ ^6H_{15/2}$	9	-5	-5/2	1/3	0.6	0.84	0.919
Ho $f^{10} \ ^5I_8$	10	-6	-2	2/15	0.8	0.813	0.964
Er $f^{11} \ ^4I_{15/2}$	11	-6	-3/2	-2/15	1.267	0.853	0.991
Tm $f^{12} \ ^3H_6$	12	-5	-1	-1/3	2	0.92	1.008
Yb $f^{13} \ ^2F_{7/2}$	13	-3	-1/2	-1/3	3	1	1

Beamline I10 is equipped with an APPLE II undulator capable of providing variable polarization [29]. To compare the results, two different undulator scanning modes were used during our experiment. The photon energy distribution of the undulator can be controlled either by changing the gap or by a shift of the upper magnet arrays with respect to the lower magnet arrays. This movement is called the jaw phase. The gap scan consists of discrete movements of the undulator, which is permanently tuned to the maximum of its emission peak.

XAS measurements were carried out in total-electron-yield (TEY) mode. The magnetic field is always along the x-ray beam direction. The Ho sample (with the normal $\parallel c$ axis) was measured at both normal ($\theta = 0^\circ$) and grazing ($\theta = 75^\circ$) incidence.

2. Computational description

Electric-dipole transitions from the $3d$ core level in rare earths are allowed to empty $4f$ states, but forbidden to $5d$ and $6s$ valence states. For the multielectronic configuration of the atom in cylindrical symmetry (SO_2), the transitions $4f^n \rightarrow 3d^9 4f^{n+1}$ are calculated using atomic multiplet theory, in which spin-orbit and electrostatic interactions are treated on an equal footing [11,30]. The intra-atomic electrostatic interactions include the $3d$ - $4f$ and $4f$ - $4f$ Coulomb and exchange interactions. The wave functions of the initial- and final-state configurations are calculated in intermediate coupling using Cowan's atomic Hartree-Fock code with relativistic corrections [31,32].

To account for interatomic screening, the parameters of the Slater integrals for the Coulomb and exchange interactions were reduced to 66%, while the spin-orbit interactions were kept at 100% [11]. The Ho M_5 line spectra were broadened by a Lorentzian of half-width at half-maximum (HWHM) of $\Gamma = 0.3$ eV for intrinsic lifetime broadening and a Gaussian of $\sigma = 0.4$ eV for instrumental broadening. The Dy M_5 spectra were broadened by a Lorentzian of $\Gamma = 0.25$ eV and Gaussian with $\sigma = 0.5$ eV.

The $4f$ wave function contraction in the heavier rare earths makes these orbitals atomic-like, with negligible influence of the local environment. Unlike the $5d$ and $6sp$ electrons, the $4f$ electrons do not participate in the chemical bonding. Therefore, the $M_{4,5}$ spectrum has essentially the same shape for metals, alloys, compounds, dopants, and oxides, apart from small differences in line broadening. Since the additional $4f$ electron is efficiently screening the $3d$ core hole, the chemical shift in the $M_{4,5}$ spectrum is small, so that differences in the XAS between rare-earth metal and oxide remain disguised. However, they can be distinguished by the magnitude of the XMCD signal, which is directly proportional to the $4f$ magnetic moment aligned along the beam [30].

For the Hund's rule ground state in LS coupling of the Ho and Dy ion, the spin, orbital, and total angular momentum (S, L, J) are found in Table I. The effective magnetic $4f$ moment, $\mu_{\text{eff}} = g_J \sqrt{J(J+1)}$, is 10.61 and 10.65 μ_B /atom for Ho and Dy, respectively, where the Landé splitting factor $g_J = 3/2 + [S(S+1) - L(L+1)]/[2J(J+1)]$.

The spectra in Fig. 1 were calculated for the Ho³⁺ $4f^{10}$ (5I_8) ground state with $M_J = -J$ in intermediate coupling at a temperature $T = 0$ K, which gives $\langle L_z \rangle = -\mu_L = -6.084$, $\langle S_z \rangle = -\frac{1}{2}\mu_S = -1.916$, and $\langle J_z \rangle = \langle L_z \rangle + \langle S_z \rangle = -8$. Thus, while the total angular momentum stays the same in intermediate coupling, the spin and orbital moment values differ slightly from the LS -coupled Hund's rule values (cf. Table I). With increasing temperature, higher magnetic sublevels M_J become populated and the magnetic moment reduces in size [33].

3. Determination of the magnetic moment

While in principle sum-rule analysis [5–7] can be used to obtain the magnetic moment in rare earths, in contrast to the $3d$ transition metals the large jj mixing between the $3d_{5/2}$ and $3d_{3/2}$ core levels and a large $\langle T_z \rangle$ make it cumbersome to extract the spin moment. Instead, we will introduce here two alternative methods, namely, (i) scaling the peak asymmetry, $A = (\mu_L - \mu_R)/(\mu_L + \mu_R)$, and (ii) fitting the experimental spectra with the three polarization components.

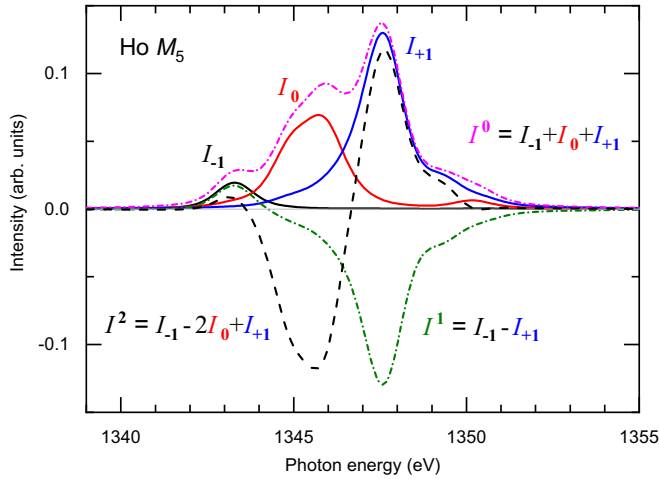


FIG. 1. Calculated XAS at the Ho M_5 edge for left-circular (I_{-1} , black solid line), right-circular (I_{+1} , blue solid line), and perpendicular linear polarization (I_0 , red solid line), together with the resulting isotropic spectrum ($I_{-1} + I_0 + I_{+1}$, pink dot-dashed line), XMCD ($I_{-1} - I_{+1}$, green dot-dashed line), and XMLD ($I_{-1} - 2I_0 + I_{+1}$, black dashed line).

We will make use of the fact that in the heavy rare earths the spin and orbital moments are parallel. This follows from a general rule which deals with the influence of a small perturbation on a J level. Using the Wigner-Eckart theorem, the proportionality rule (given in Eq. (32) of Ref. [34]) states that different operators of the same rank are all proportional to the same tensor. For tensors of rank 1 this implies that the orbital moment $\langle L \rangle$, spin moment $\langle S \rangle$, and magnetic dipole term $\langle T \rangle$, are proportional to the total angular momentum $\langle J \rangle$. Then, these vectors are parallel and have a constant ratio, independent of a small perturbation, such as crystal-field interaction. This makes it of course less essential to apply the sum rules since the orbital over spin ratio is fixed anyway.

In Ho the energy separation between the ground-state level ($J = 8$) and the first excited level ($J = 7$) is ~ 673 meV ≈ 7800 K. In Dy this energy separation between the lower levels $J = 15/2$ and $13/2$ is ~ 469 meV ≈ 5450 K. These splittings are at least an order of magnitude larger than the $4f$ crystal-field splitting [35]. When the crystal field becomes of the order of the spin-orbit coupling, other J levels will mix into the ground state, and the moments are no longer proportional to each other. The proportionality rule also applies to intermediate coupling [34], since J is a good quantum number as long as the crystal field is much smaller than the electrostatic and spin-orbit interactions. The proportionality rule obviously does not hold to $3d$ transition metals, where the crystal field is much stronger than the spin-orbit interaction.

IV. THEORY

A. XMCD

1. Polarized spectra

Figure 1 shows the spectra I_q calculated in SO_2 symmetry, for left-circular ($q = -1$), right-circular ($q = +1$), and perpendicular linear polarization ($q = 0$), together with the

linear combinations of those spectra,

$$\begin{aligned} I^0 &= I_{-1} + I_0 + I_{+1}, \\ I^1 &= I_{-1} - I_{+1}, \\ I^2 &= I_{-1} - 2I_0 + I_{+1}, \end{aligned} \quad (8)$$

which are the isotropic spectrum, XMCD, and XMLD, respectively, and are often called the *fundamental spectra*. Reversely, this can be written as

$$I_{\pm 1} = \frac{1}{3}I^0 \mp \frac{1}{2}I^1 + \frac{1}{6}I^2, \quad (9)$$

$$I_0 = \frac{1}{3}I^0 - \frac{1}{3}I^2. \quad (10)$$

It is important to note that the *perpendicular* linear polarization for I_0 is taken along the beam direction of the circular polarization. Since light is transversely polarized, this can only be achieved by changing the sample orientation with respect to the incident x-ray beam. Thus, the perpendicular linear polarized spectrum I_0 should not be confused with the parallel linear polarized spectrum,

$$I_{\parallel} \equiv \frac{1}{2}(I_{-1} + I_{+1}) = \frac{1}{3}I^0 + \frac{1}{6}I^2. \quad (11)$$

The aim is to relate the calculated spectra I_q to the experimental spectra, which for distinction are named μ_L , μ_Z , and μ_R . The spectra with (anti)parallel alignment are

$$\begin{aligned} \mu^{\uparrow\downarrow} &\approx \mu_{L,B} \approx \mu_{R,-B}, \\ \mu^{\uparrow\uparrow} &\approx \mu_{R,B} \approx \mu_{L,-B}, \\ \mu_{Z,B} &\approx \mu_{Z,-B}, \end{aligned} \quad (12)$$

where the subscripts L and R correspond to negative and positive photon helicity, respectively, and the subscript $\pm B$ gives the direction of the applied field with respect to the helicity vector. In Eq. (12) we use an approximate sign (\approx) because the degree of polarization and degree of magnetization can be different upon reversal. When these remain the same this becomes an equal sign. Then, reversal of both field and helicity results in the same XMCD signal. The μ_Z is the perpendicular linear polarized spectrum, which is even in the magnetization, i.e., it should be the same for parallel and antiparallel alignment of linear polarization and field.

The convention adopted by the XMCD community is to plot the circular dichroism of the transition-metal L_3 peak and rare-earth M_5 peak as having negative integrated intensity [4]. This corresponds to an XMCD signal, $\Delta\mu$, defined as the difference between antiparallel and parallel orientations of photon helicity and sample magnetization,

$$\begin{aligned} \Delta\mu &\equiv \mu^{\uparrow\downarrow} - \mu^{\uparrow\uparrow} \\ &\approx (\mu_{L,B} - \mu_{R,B}) \approx (\mu_{R,-B} - \mu_{L,-B}) \\ &\approx (\mu_{L,B} - \mu_{L,-B}) \approx (\mu_{R,-B} - \mu_{R,B}). \end{aligned} \quad (13)$$

To recapitulate the sign convention, a magnetic atom aligned along B_z has a positive magnetic moment \mathcal{M}_z , negative $\langle J_z \rangle = \langle M \rangle = \sum_M n_M M$, and by definition a negative dichroism $\Delta\mu = \mu_{L,B} - \mu_{R,B}$.

In the following, we do not take for granted that the degree of polarization in the experimental spectra μ stays the same upon reversal of the helicity or magnetization but instead that it can be different.

2. Method of using the peak asymmetry

Under the condition that the $4f$ crystalline electrostatic field is small compared to the $4f$ spin-orbit interaction, the spin and orbital moments remain parallel, so that their ratio is fixed. Then, as a function of magnetization the isotropic spectrum remains constant and the XMCD and XMLD scale with factors c_Q as

$$\begin{aligned} c_0 I^0 &= \mu^0, \\ c_1 I^1 &= \mu^1, \\ c_2 I^2 &= \mu^2, \end{aligned} \quad (14)$$

where μ^0 , μ^1 , and μ^2 are the experimental isotropic spectrum, XMCD, and XMLD, respectively. There is an arbitrary scaling factor between the set of theoretical and experimental spectra in Eq. (14). Therefore, the μ^0 spectrum can be normalized to I^0 by taking $c_0 = 1$. We will use this normalization from here on, but often still explicitly write c_0 in order to keep track of this coefficient.

The scaling factor for the measured dichroism can be directly obtained from the normalized asymmetry, i.e., the ratio XMCD/XAS,

$$\frac{c_1}{c_0} = \frac{\mu^1 I^0}{\mu^0 I^1}. \quad (15)$$

Thus, the actual circular dichroism is c_1/c_0 times that of the calculated XMCD spectrum I^1 . Instead, one could also compare the asymmetry against that of a reference sample with known magnetic moment. This has the advantage that no spectral calculations are required, just as in the case of the sum rules. This method of analyzing the peak asymmetry has been applied in Refs. [19], [24], and [36], therefore we will not further elaborate on it. The problem with this method remains that for practical reasons one usually takes the peak asymmetry, $A = (\mu_L - \mu_R)/(\mu_L + \mu_R)$, instead of μ^1/μ^0 , so the contribution of μ_Z in the denominator is omitted, which amounts to neglecting the linear dichroism. To remediate this shortcoming, we will describe in the next subsection an alternative method which explicitly takes into account the linear dichroism.

3. Method of using the fitted spectra

Similar to the calculated spectra in Eq. (9), we can express the experimental spectrum μ with arbitrary polarization as a linear combination of fundamental spectra,

$$\mu = \frac{1}{3}\mu^0 + \frac{1}{2}\mu^1 + \frac{1}{6}\mu^2 = \frac{1}{3}c_0 I^0 + \frac{1}{2}c_1 I^1 + \frac{1}{6}c_2 I^2. \quad (16)$$

The value of c_1 is taken positive for antiparallel alignment ($\mu_{L,B}$ and $\mu_{R,-B}$) and negative for parallel alignment ($\mu_{R,B}$ and $\mu_{L,-B}$).

It is important to note that Eq. (14) means that c_1 and c_2 correspond to the degree of circular and linear dichroism, respectively, in the measured spectra, with respect to the calculated spectra.

The spectrum μ can also be written as a linear combination of the three calculated polarized spectra

$$\mu = \sum_q a_q I_q = a_{-1} I_{-1} + a_0 I_0 + a_{+1} I_{+1}, \quad (17)$$

where $a_q \geq 0$ and $\sum_q a_q = 1$.

Substituting Eqs. (9) and (10) into Eq. (17) and comparing the result to Eq. (16) gives the dichroism coefficients c_Q in terms of polarization coefficients a_q as

$$\begin{aligned} c_0 &= a_{-1} + a_0 + a_{+1} = 1, \\ c_1 &= a_{-1} - a_{+1}, \\ c_2 &= a_{-1} - 2a_0 + a_{+1} = 1 - 3a_0. \end{aligned} \quad (18)$$

Reversely, we can write

$$\begin{aligned} a_{\pm 1} &= \frac{1}{3}c_0 \mp \frac{1}{2}c_1 + \frac{1}{6}c_2, \\ a_0 &= \frac{1}{3}c_0 - \frac{1}{3}c_2. \end{aligned} \quad (19)$$

Substitution of Eq. (19) into (17) gives the relation

$$\begin{aligned} \mu &= \left(\frac{1}{3}c_0 + \frac{1}{2}c_1 + \frac{1}{6}c_2\right)I_{-1} + \left(\frac{1}{3}c_0 - \frac{1}{3}c_2\right)I_0 \\ &+ \left(\frac{1}{3}c_0 - \frac{1}{2}c_1 + \frac{1}{6}c_2\right)I_{+1}. \end{aligned} \quad (20)$$

It can be immediately verified that with $c_0 = 1$, $c_1 = \pm 1$, and $c_2 = 1$ we obtain $\mu = I_{\mp 1}$.

Since the weights a_q of the polarized spectra have to be positive, Eq. (19) gives the conditions

$$-\frac{1}{2}c_0 \leq c_2 \leq c_0 \quad \text{and} \quad |c_1| \leq \frac{2}{3}c_0 + \frac{1}{3}c_2. \quad (21)$$

The latter shows that if $c_2 = 0$ (no linear dichroism) then $|c_1| \leq \frac{2}{3}$, which means the circular dichroism cannot reach its full strength. The explanation behind this restriction comes from the fact that light is a transverse wave, so that $I_{\pm 1}$ also contains I^2 [cf. Eq. (9)]. This shows that we explicitly have to include the linear dichroism in the circularly polarized spectra. This is especially important for the rare earths where the linear dichroism is usually quite large. It is less important for $3d$ transition metals with a small linear dichroism.

On the other hand, if $c_1 = 0$ (no circular dichroism) then there is no restriction on c_2 , because the linear spectra as given in Eqs. (10) and (11) do not contain I^1 .

Finally, we describe how this method is implemented in Sec. V. The theoretical spectra I_q were calculated under full light polarization and magnetization conditions. To determine the circular dichroism of the individual experimental spectra μ they were fitted with a linear combination of the theoretical spectra I_{-1} , I_0 , and I_{+1} , as expressed by Eq. (17). Prior to fitting the experimental spectra, the theoretical spectra were first corrected for saturation effects (as described in Sec. IV B). The coefficients a_q were then obtained from the original unsaturated I_q spectra. Using Eq. (18), these polarization coefficients a_q give the dichroism coefficients c_1 and c_2 , which are the scaling factors of the measured spectra compared to the calculated circular and linear dichroism, cf. Eq. (14). Comparing the results for the different individual spectra measured with left- and right-circular polarization or with positive and negative field allows us to determine the consistency of the results for opposite geometries.

B. Saturation effects

Since the $3d \rightarrow 4f$ cross section is large and also very different for each polarization, we need to account for the saturation effects in the TEY spectrum that arise because the x-ray attenuation length, $\Lambda = 1/\mu$, is comparable in length

TABLE II. Optical constants for Ho and Dy.

	E (eV)	c_{RE}	$\Lambda_{TI}^{\text{Henke}}$ (nm)	$\Lambda_{RE}^{\text{Henke}}$ (nm)	$\Lambda_{RE, M_5 \text{max}}^{\text{Thole}}$ (nm)	L (nm)
Ho M_5	1348.1	0.055	261	742	10.7	6
Dy M_5	1292.9	0.1125	245	731	12.7	6

to the electron escape depth L [4]. The reduction factor of the TEY spectrum due to saturation is photon energy (E) dependent and given by [11,37]

$$\frac{\mu_{\text{sat}}}{\mu_{\text{unsat}}} = \frac{\cos \theta}{\cos \theta + L\mu_{\text{tot}}(E)}, \quad (22)$$

where θ is the incidence angle from the surface normal. The total x-ray absorption is

$$\mu_{\text{tot}}(E) = (1 - c_{RE}) \mu_{TI} + c_{RE} \mu_{RE}(E), \quad (23)$$

$$\mu_{TI} = \frac{1}{\Lambda_{TI}^{\text{Henke}}}, \quad (24)$$

$$\mu_{RE}(E) = \frac{1}{\Lambda_{RE}^{\text{Henke}}} + \frac{\mu_{\text{calc}}(E)}{\mu_{RE, M_5 \text{max}}^{\text{calc}}} \frac{1}{\Lambda_{RE, M_5 \text{max}}^{\text{Thole}}}, \quad (25)$$

where c_{RE} is the concentration of the RE. The nonresonant attenuation lengths Λ^{Henke} can be taken from Henke's data tables [38], available at the Center for X-Ray Optics (CXRO) website [39]. The second term in Eq. (23) contains the calculated unsaturated absorption spectrum $\mu_{\text{calc}}(E)$, which is normalized to the maximum of the M_5 peak $\mu_{RE, M_5 \text{max}}^{\text{calc}}$ and scaled to the resonant absorption length $\Lambda_{RE, M_5 \text{max}}^{\text{Thole}}$ as given by Thole *et al.* [11], from which we also adopt the value of the electron escape depth L . The values required for the Dy and Ho M_5 are given in Table II.

Saturation effects become stronger for higher doping concentration, although even the pure rare-earth metals can be fully corrected [11]. For the Ho ($x = 0.14$) sample, Eq. (22) gives an intensity reduction to 83% and 95% at the M_5 peak maximum for grazing incidence ($\theta = 75^\circ$) and normal incidence ($\theta = 0^\circ$), respectively.

V. APPLICATION

A. Holmium results

Figure 1 shows the polarization components of the Ho M_5 edge which are well separated in energy. The main peak at 1347.5 eV is almost purely I_{+1} with only a few percent of I_0 . The M_4 signal is much smaller and less suitable, so it is not considered here, although its measured XAS and XMCD are in good agreement with multiplet calculations [11].

The experimental Ho M_5 spectra with positive ($\mu_{R,B}$) and negative helicity ($\mu_{L,B}$) were fitted using the calculated I_{-1} , I_0 , and I_{+1} spectra from Fig. 1. For normal incidence, the results are shown in Fig. 2, where fitting gives the coefficients a_q [defined in Eq. (17)] listed in Table III together with the resulting c_1 and c_2 values [using Eq. (18)]. This shows that the experimental spectra are far from being fully polarized. Despite this, the spectra are very similar to other polarized Ho spectra from the literature [40].

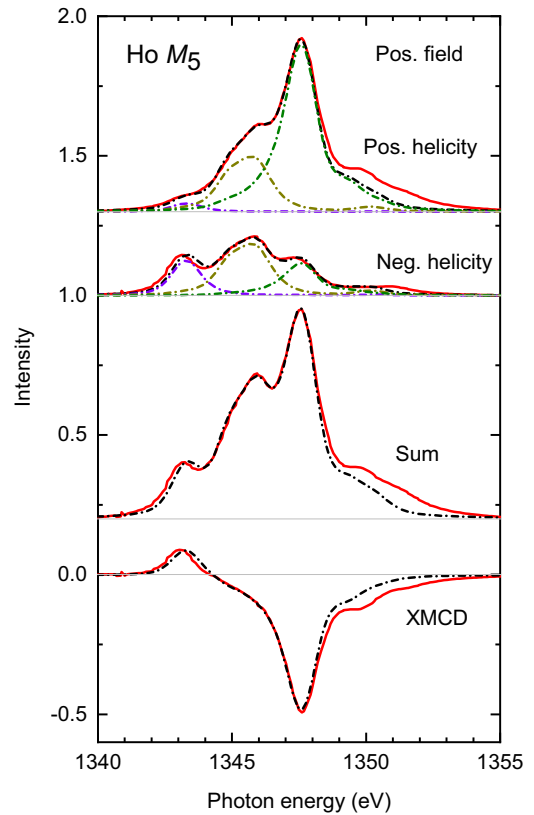


FIG. 2. Experimental Ho M_5 spectra (drawn red lines) for positive and negative helicity and their sum and difference spectra compared with the calculated spectra (dash-dotted black lines). The experimental spectra were measured at 2.5 K and 7 T at normal incidence in TEY mode. They were fitted with the I_{-1} , I_0 , and I_{+1} spectra from Fig. 1, which were corrected for saturation effects using Eq. (22), yielding the intensity ratios analyzed by Eq. (20), which amounts to an XMCD effect of 45%. The fit results are listed in Table III. The I_{-1} , I_0 , and I_{+1} components are peaking around 1343, 1345.5, and 1347.5 eV, respectively.

Also listed in Table III are the results from fitting the experimental spectra at grazing incidence (spectra not shown) and their corresponding c_1 and c_2 values.

For both normal and grazing incidence geometry of Ho (Table III) there is a large difference in $|c_1|$ between μ_L and μ_R . On the other hand, these two different incidence geometries give similar c_1 values for μ_L as well as similar c_1 values for μ_R .

TABLE III. Coefficients a_q of the fitted I_q spectra and resulting values of c_1 and c_2 for Ho M_5 XAS spectra with left- and right-circular polarization at normal and grazing incidence in positive magnetic field and undulator jaw scans.

	a_{-1}	a_0	a_{+1}	c_1	c_2
$\mu_{L,B}$ (norm. inc.)	0.6385	0.2743	0.0872	0.5513	0.1771
$\mu_{R,B}$ (norm. inc.)	0.1606	0.3212	0.5181	-0.3575	0.0364
$\mu_{L,B}$ (graz. inc.)	0.6623	0.2529	0.0848	0.5775	0.2413
$\mu_{R,B}$ (graz. inc.)	0.1780	0.3089	0.5131	-0.2413	0.0733

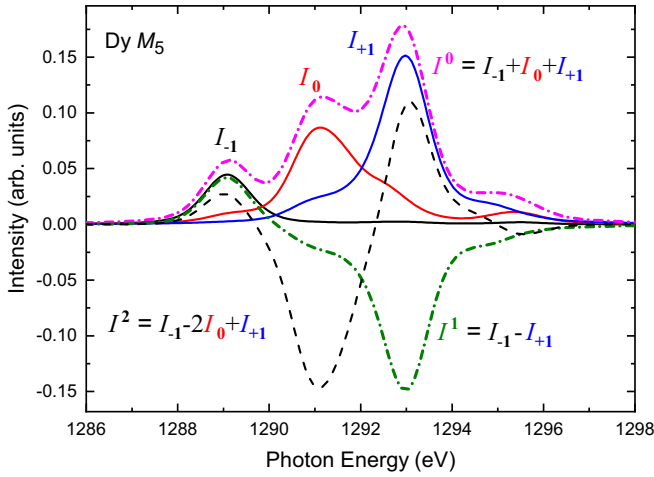


FIG. 3. Calculated XAS at the Dy M_5 edge for left-circular (I_{-1} , black solid line), right-circular (I_{+1} , blue solid line) and perpendicular linear polarization (I_0 , red solid line), together with the resulting isotropic spectrum ($I_{-1} + I_0 + I_{+1}$, pink dot-dashed line), XMCD ($I_{-1} - I_{+1}$, green dot-dashed line) and XMLD ($I_{-1} - 2I_0 + I_{+1}$, black dashed line).

Furthermore, we found no noticeable difference between XAS spectra measured with linear polarization in normal and grazing incidence. This suggests there is no significant crystal-field interaction such as reported for Dy overlayers in the absence of any magnetic field [41–43]. Calculations taking into account $4f$ crystal-field interaction show only a small reduction in the dichroism signal, so that crystal field is not expected to be the culprit.

As mentioned, c_1 gives the degree of circular dichroism in the measured spectrum, where $c_1 = 1$ is reached under full polarization and magnetization as in the calculated spectra for the Hund's rule ground state. Using the average value over μ_L and μ_R from Table III for normal incidence and grazing incidence, $|c_1|$ is equal to 0.45 and 0.41, respectively, which would correspond to an effective magnetic moment $\mu_{\text{eff}} \approx 4.8 \mu_B$ if the beam was fully polarized, which as we show in Sec. VB is likely not the case. The reduced magnetic moment can be ascribed to nonmagnetic or antiferromagnetic Ho sites. This could be due to oxidation, since the TEY detection is rather surface sensitive with an electron escape depth of 6 nm. Simultaneously with the TEY, we also measured in fluorescence yield detection. However, the latter spectra show very strong saturation effects, hampering the extraction of quantitative information. Hence, it seems that not all Ho moments are aligned to the field. This agrees with EXAFS results that show distinct amounts of oxidation of the rare-earth dopants [44].

B. Dysprosium results

The calculated Dy M_5 spectra are displayed in Fig. 3. For normal incidence, the fit results are shown in Fig. 4. We compared both undulator jaw and gap scans as well as positive and negative magnetic field (± 5 T). The results for a_q are collected in Table IV together with the corresponding c_1 and c_2 values.

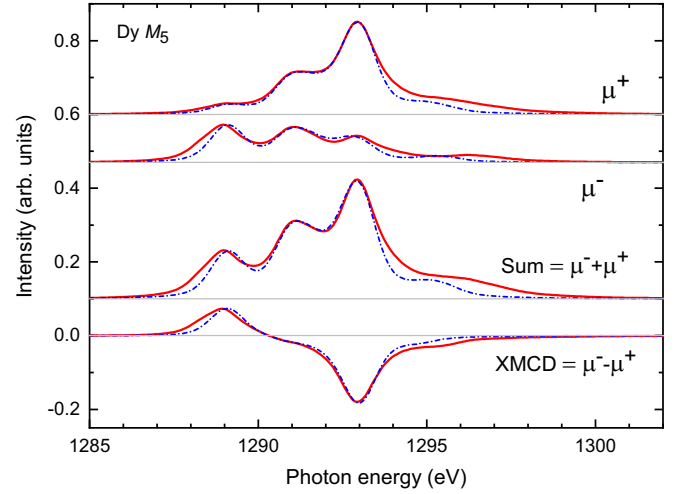


FIG. 4. Experimental Dy M_5 spectra (drawn red lines) for positive and negative helicity and their sum and difference spectra compared with the calculated spectra (dash-dotted black lines). The experimental spectra were measured at 2.5 K and 7 T at normal incidence in TEY mode. The calculated spectra are fits using the I_{-1} , I_0 , and I_{+1} spectra from Fig. 3, which were corrected for saturation effects using Eq. (22). The fit results are listed in Table IV. The I_{-1} , I_0 , and I_{+1} components are peaking around 1289, 1291, and 1293 eV, respectively.

Reversing the field gives consistent results showing a reversal of the sign of c_1 [e.g., $c_1(\mu_{L,B}) = -c_1(\mu_{L,-B})$ in Table IV]. However, this cannot be said for reversing the helicity [e.g., $c_1(\mu_{L,B}) \neq -c_1(\mu_{R,B})$ in Tables III and IV]. Thus, reversing the field gives more consistent results than reversing the light polarization. Interestingly, jaw and gap scans of the undulator give very similar results. The values for Dy averaged over all μ are $|c_1| = 0.4170$ and $c_2 = -0.0248$.

Collecting all results for Dy from Table IV, averaged over undulator modes and field directions but distinguished by light helicity, gives

$$\begin{aligned} \text{all } \mu_L: |c_1| &= 0.4652 \pm 0.0094; c_2 = -0.0287 \pm 0.0115, \\ \text{all } \mu_R: |c_1| &= 0.3687 \pm 0.0156; c_2 = -0.0209 \pm 0.0227, \end{aligned} \quad (26)$$

TABLE IV. Coefficients a_q of the fitted I_q spectra and resulting values of c_1 and c_2 for Dy M_5 XAS spectra with left- and right-circular polarization at normal incidence in positive and negative magnetic field and undulator jaw and gap scans, as indicated.

	a_{-1}	a_0	a_{+1}	c_1	c_2
$\mu_{L,B}$ (jaw)	0.5584	0.3469	0.0948	0.4636	-0.0407
$\mu_{L,-B}$ (jaw)	0.0957	0.3397	0.5646	-0.4689	-0.0191
$\mu_{L,B}$ (gap)	0.5567	0.3448	0.0985	0.4582	-0.0344
$\mu_{L,-B}$ (gap)	0.0950	0.3400	0.5650	-0.4700	-0.0200
$\mu_{R,-B}$ (jaw)	0.5137	0.3495	0.1368	0.3769	-0.0485
$\mu_{R,B}$ (jaw)	0.1397	0.3445	0.5158	-0.3761	-0.0335
$\mu_{R,-B}$ (gap)	0.5114	0.3379	0.1507	0.3607	-0.0137
$\mu_{R,B}$ (gap)	0.1548	0.3293	0.5159	-0.3611	0.0121

which means that there is a difference of $\sim 20\%$ in the relative degree of circular dichroism between the left and right polarized beam.

For the spectra averaged over the light polarization but distinguished by field direction we obtain

$$\begin{aligned} \text{all } \mu_B: |c_1| &= 0.4148 \pm 0.0930; c_2 = -0.0241 \pm 0.0422, \\ \text{all } \mu_{-B}: |c_1| &= 0.4191 \pm 0.1013; c_2 = -0.0253 \pm 0.0272, \end{aligned} \quad (27)$$

which amounts to a difference of only 1% in magnetic dichroism between the two opposite magnetizations.

Whether or not reversing the field gives the same degree of dichroism is specific to the nature of the sample. For instance, in the case of magnetic domain structure the magnetization reversal might be incomplete at low fields. For our samples the consistency of the magnetization reversal is supported by the SQUID measurements, which show a paramagnetic behavior with full magnetic saturation at 5 T [25].

Some years earlier the degree of the circular polarized light of the beamline was measured using an x-ray polarimeter and reported to be close to 100% [45]. However, its performance can have deteriorated over the years. Furthermore, switching the helicity of the exciting radiation can cause slight shifts of the beam spot on the sample surface, illuminating other areas on the surface, which could possibly lead to a difference. However, the samples were rather homogeneous across the surface. Hence, the reduced values of $|c_1|$ compared to the theoretical results should not only be ascribed to a reduced magnetization but can also partly originate from an incomplete circular polarization of the x-ray beam.

C. Influence of the XMLD on the XMCD

To finish off, we discuss the effect of the XMLD on the experimental XMCD, which is the difference spectrum μ^1 . From Eqs. (17) and (16) we obtain sequentially

$$\begin{aligned} \mu^1 &= \mu_L - \mu_R \\ &= (a_{-1}^L - a_{-1}^R)I_{-1} + (a_0^L - a_0^R)I_0 + (a_{+1}^L - a_{+1}^R)I_{+1} \\ &= \left(\frac{c_0^L - c_0^R}{3}\right)I^0 + \left(\frac{c_1^L - c_1^R}{2}\right)I^1 + \left(\frac{c_2^L - c_2^R}{6}\right)I^2, \end{aligned} \quad (28)$$

where the spectra measured with left (L) and right (R) circular polarization are characterized by polarization components

$a_q^{L,R}$ and dichroism components $c_Q^{L,R}$. The μ and I spectra are photon energy dependent, whereas the coefficients a_q and c_Q have fixed values. Looking at the bottom line in Eq. (28), the first term expresses the requirement for proper normalization of the isotropic spectra. The second term is the usual one, showing that the XMCD is proportional to the averaged absolute degree of circular dichroism. Note that c_1^L and c_1^R are positive and negative, respectively. The third term gives the contribution of the linear dichroism I^2 , which is proportional to the mismatch in the degree of linear dichroism between both spectra.

A further contribution from the linear dichroism arises in the application of the sum rules, which formally requires the normalization of the XMCD by the isotropic spectrum that contains the perpendicular linear polarized spectrum.

The integrated linear dichroism is proportional to the orbital charge anisotropy [46]. This can be very large for localized $4f$ states [47] but is often smaller for metallic $3d$ transition metal states, especially in cubic symmetry [32].

VI. CONCLUSIONS

One of the shortcomings in obtaining the magnetic circular dichroism as a difference spectrum is that it does not take into account that the individual spectra can have been measured with different degrees of polarization and magnetization. By analyzing the individual polarized XAS spectra measured at the Ho and Dy M_5 edges without taking the difference spectrum, we are able to determine the differences in the degree of circular dichroism of these spectra. In the experiments on our paramagnetic samples we found that reversing the field gives more consistent results than reversing the circular polarization.

We show that since light is a transverse wave, the circularly polarized spectra cannot be fitted just by the isotropic spectrum and the circular dichroism, but also requires the linear dichroism to be included. Only a fit of the experimental spectra by three polarization components can give accurate results in the case of the rare earths.

ACKNOWLEDGMENT

We acknowledge the Diamond Light Source for time on beamline I10 awarded under Proposal No. SI-10207.

-
- [1] B. T. Thole, G. van der Laan, and G. A. Sawatzky, *Phys. Rev. Lett.* **55**, 2086 (1985).
 - [2] G. van der Laan, B. T. Thole, G. A. Sawatzky, J. B. Goedkoop, J. C. Fuggle, J. M. Esteva, R. C. Karnatak, J. P. Remeika, and H. A. Dabkowska, *Phys. Rev. B* **34**, 6529 (1986).
 - [3] G. Schütz, W. Wagner, W. Wilhelm, P. Kienle, R. Zeller, R. Frahm, and G. Materlik, *Phys. Rev. Lett.* **58**, 737 (1987).
 - [4] G. van der Laan and A. I. Figueroa, *Coord. Chem. Rev.* **277-278**, 95 (2014).
 - [5] B. T. Thole, P. Carra, F. Sette, and G. van der Laan, *Phys. Rev. Lett.* **68**, 1943 (1992).
 - [6] P. Carra, B. T. Thole, M. Altarelli, and X. Wang, *Phys. Rev. Lett.* **70**, 694 (1993).
 - [7] G. van der Laan, *Phys. Rev. B* **57**, 112 (1998).
 - [8] F. Schäfers, H.-C. Mertins, A. Gaupp, W. Gudat, M. Mertin, I. Packe, F. Schmolla, S. Di Fonzo, G. Soullié, W. Jark, R. Walker, X. Le Cann, R. Nyholm, and M. Eriksson, *Appl. Opt.* **38**, 4074 (1999).
 - [9] J. B. Kortright, M. Rice, and K. D. Franck, *Rev. Sci. Instrum.* **66**, 1567 (1995).
 - [10] B. T. Thole and G. van der Laan, *Phys. Rev. B* **38**, 3158 (1988).
 - [11] B. T. Thole, G. van der Laan, J. C. Fuggle, G. A. Sawatzky, R. C. Karnatak, and J. M. Esteva, *Phys. Rev. B* **32**, 5107 (1985).
 - [12] G. van der Laan, *J. Synchrotron Rad.* **6**, 694 (1999).

- [13] C. T. Chen, Y. U. Idzerda, H.-J. Lin, N. V. Smith, G. Meigs, E. Chaban, G. H. Ho, E. Pellegrin, and F. Sette, *Phys. Rev. Lett.* **75**, 152 (1995).
- [14] K. W. Edmonds, N. R. S. Farley, T. K. Johal, G. van der Laan, R. P. Champion, B. L. Gallagher, and C. T. Foxon, *Phys. Rev. B* **71**, 064418 (2005).
- [15] A. I. Figueroa, G. van der Laan, L. J. Collins-McIntyre, S.-L. Zhang, A. A. Baker, S. E. Harrison, P. Schonherr, G. Cibin, and T. Hesjedal, *Phys. Rev. B* **90**, 134402 (2014).
- [16] Y. Teramura, A. Tanaka, B. T. Thole, and T. Jo, *J. Phys. Soc. Jpn.* **65**, 3056 (1996).
- [17] C. L. Kane and E. J. Mele, *Phys. Rev. Lett.* **95**, 146802 (2005).
- [18] B. A. Bernevig, T. L. Hughes, and S.-C. Zhang, *Science* **314**, 1757 (2006).
- [19] M. Watson, L. J. Collins-McIntyre, A. Coldea, D. Prabhakaran, L. R. Shelford, S. C. Speller, T. Mousavi, C. Grovenor, Z. Salman, S. R. Giblin, G. van der Laan, and T. Hesjedal, *New J. Phys.* **15**, 103016 (2013).
- [20] L. J. Collins-McIntyre, M. D. Watson, A. A. Baker, S. L. Zhang, A. I. Coldea, S. E. Harrison, A. Pushp, A. J. Kellock, S. S. P. Parkin, G. van der Laan, and T. Hesjedal, *AIP Adv.* **4**, 127136 (2014).
- [21] L. J. Collins-McIntyre, S. E. Harrison, P. Schoenherr, N.-J. Steinke, C. J. Kinane, T. R. Charlton, D. Alba-Venero, A. Pushp, A. J. Kellock, S. S. P. Parkin, J. S. Harris, S. Langridge, G. van der Laan, and T. Hesjedal, *Europhys. Lett.* **107**, 57009 (2014).
- [22] L. J. Collins-McIntyre, L. B. Duffy, A. Singh, N.-J. Steinke, C. J. Kinane, T. R. Charlton, A. Pushp, A. J. Kellock, S. S. P. Parkin, C. H. W. Barnes, G. van der Laan, S. Langridge, and T. Hesjedal, *Europhys. Lett.* **115**, 27006 (2016).
- [23] L. B. Duffy, A. I. Figueroa, L. Gladczuk, N.-J. Steinke, K. Kummer, G. van der Laan, and T. Hesjedal, *Phys. Rev. B* **95**, 224422 (2017).
- [24] S. E. Harrison, L. J. Collins-McIntyre, S. Li, A. A. Baker, L. R. Shelford, Y. Huo, A. Pushp, S. S. P. Parkin, J. S. Harris, E. Arenholz, G. van der Laan, and T. Hesjedal, *J. Appl. Phys.* **115**, 023904 (2014).
- [25] S. E. Harrison, L. J. Collins-McIntyre, S.-L. Zhang, A. A. Baker, A. I. Figueroa, A. J. Kellock, A. Pushp, S. S. P. Parkin, J. S. Harris, G. van der Laan, and T. Hesjedal, *Appl. Phys. Lett.* **107**, 182406 (2015).
- [26] A. I. Figueroa, S. E. Harrison, L. J. Collins-McIntyre, G. van der Laan, and T. Hesjedal, *Phys. Status Solidi RRL* **10**, 467 (2016).
- [27] S. E. Harrison, L. J. Collins-McIntyre, S.-L. Zhang, A. A. Baker, A. I. Figueroa, A. J. Kellock, A. Pushp, S. S. P. Parkin, J. S. Harris, G. van der Laan, and T. Hesjedal, *J. Phys.: Condens. Matter* **27**, 245602 (2015).
- [28] A. I. Figueroa, A. A. Baker, S. E. Harrison, K. Kummer, G. van der Laan, and T. Hesjedal, *J. Magn. Magn. Mater.* **422**, 93 (2017).
- [29] T. Schmidt and D. Zimoch, *AIP Conf. Proc.* **879**, 404 (2007).
- [30] G. van der Laan, *Lect. Notes Phys.* **697**, 143 (2006).
- [31] R. D. Cowan, *The Theory of Atomic Structure and Spectra* (University of California Press, Berkeley, 1981).
- [32] G. van der Laan and B. T. Thole, *Phys. Rev. B* **43**, 13401 (1991).
- [33] G. van der Laan and B. T. Thole, *Phys. Rev. B* **42**, 6670 (1990).
- [34] G. van der Laan and B. T. Thole, *Phys. Rev. B* **53**, 14458 (1996).
- [35] J. B. Gruber, G. W. Burdick, U. V. Valiev, K. L. Nash, S. A. Rakhimov, and D. K. Sardar, *J. Appl. Phys.* **106**, 113110 (2009).
- [36] K. W. Edmonds, G. van der Laan, and G. Panaccione, *Semicond. Sci. Technol.* **30**, 043001 (2015).
- [37] G. Van Der Laan and B. T. Thole, *J. Electron Spectrosc. Relat. Phenom.* **46**, 123 (1988).
- [38] B. L. Henke, P. Lee, T. J. Tanaka, R. L. Shimabukuro, and B. K. Fujikawa, *At. Data Nucl. Data Tables* **27**, 1 (1982).
- [39] CXRO website: cxro.lbl.gov.
- [40] F. Donati, A. Singha, S. Stepanow, C. Wackerlin, J. Dreiser, P. Gambardella, S. Rusponi, and H. Brune, *Phys. Rev. Lett.* **113**, 237201 (2014).
- [41] M. Sacchi, O. Sakho, and G. Rossi, *Phys. Rev. B* **43**, 1276 (1991).
- [42] M. Sacchi, F. Sirotti, G. Rossi, R. J. H. Kappert, J. Vogel, and J. C. Fuggle, *J. Electron Spectrosc. Relat. Phenom.* **58**, 393 (1992).
- [43] R. J. H. Kappert, J. Vogel, M. Sacchi, and J. C. Fuggle, *Phys. Rev. B* **48**, 2711 (1993).
- [44] A. I. Figueroa, G. van der Laan, S. E. Harrison, G. Cibin, and T. Hesjedal, *Sci. Rep.* **6**, 22935 (2016).
- [45] H. Wang, P. Bencok, P. Steadman, E. Longhi, J. Zhu, and Z. Wang, *J. Synchrotron Rad.* **19**, 944 (2012).
- [46] G. van der Laan, *Phys. Rev. Lett.* **82**, 640 (1999).
- [47] J. B. Goedkoop, B. T. Thole, G. van der Laan, G. A. Sawatzky, F. M. F. de Groot, and J. C. Fuggle, *Phys. Rev. B* **37**, 2086 (1988).